ACS OMEGA

http://pubs.acs.org/journal/acsodf

Article

Promoting Visible Light Generation of Hydrogen Using a Sol–Gel-Prepared $MnCo_2O_4$@g-C_3N_4 p–n Heterojunction Photocatalyst

Maha Alhaddad, Reda M. Mohamed,* and Mohamed H. H. Mahmoud

Cite This: *ACS Omega* 2021, 6, 8717–8725

Read Online

ACCESS | Metrics & More | Article Recommendations

ABSTRACT: The production of hydrogen using a new type of heterogeneous photocatalyst under visible light is considered a remarkable essential pathway for sustainable, pure energy not only on the laboratory scale but also on a bigger scale. Hence, a new nanocomposite of mesoporous $MnCo_2O_4$, g-C_3N_4, and $MnCo_2O_4$@g-C_3N_4 was produced utilizing a sol–gel method with variable $MnCo_2O_4$ contents. The crystal structure of $MnCo_2O_4$ was effectively confirmed by the X-ray diffraction pattern and integrated onto the g-C_3N_4 structure. The $MnCo_2O_4$ nanoparticles were displayed as spherical particles by TEM images and dispersed in a uniform way inside the g-C_3N_4 nanosheet. The synthesized nanocomposites in the form of $MnCo_2O_4$@g-C_3N_4 were examined as a new effective photocatalyst against glycerol as a source for H_2 production with visible light. The $MnCo_2O_4$ contents indicated a corroborative impact for the photocatalytic action related to the H_2 production process. A maximum H_2 production molecular value was observed (21,870 μmol·g^{-1}·h^{-1}) for a 1.5 wt % $MnCo_2O_4$@g-C_3N_4 nanocomposite as a considerable increase in its photocatalytic activity. The yields of H_2 are ∼55 and 23 times higher than those of g-C_3N_4 and $MnCo_2O_4$, respectively. Up to five times cycles of visible lighting were the maximum number of repeated cycles by which the 1.5 wt % $MnCo_2O_4$@g-C_3N_4 product showed higher stability and durability.

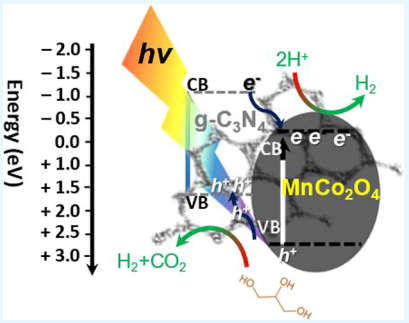

1. INTRODUCTION

The recent technological development in the field of photocatalytic activity of a variable type of new material based on solar light is reflected in a widely convenient way to convert energy for environmental curing and even for the organic synthesis methodology.[1,2] A particular one is the reaction of H_2 production in the presence of nanomaterials containing different semiconductor types with variable approximate electron donor types. The major renewable source for clean energy depends on the specific type of material such as carbohydrates and alcohol. This fact has been recognized in the existence of a visible light illumination source.[3,4] In general, any developed oxidation process such as the photocatalytic effects of any heterogeneous catalyst reaction is most likely wastewater processing for pollutant regression.[5,6] In a more enjoyable manner, the photocatalytic reaction utilizes the sunlight renewable energy source together with the existence of a heterogeneous catalyst to produce a clean environment without any additional minor pollutants. This is mainly due to the complete mineralization process in water, carbon dioxide, and any other suitable inorganic ions from its primary organic pollutants.[7] The functional wastewater processing in the presence of variable types of semiconductors for the disintegration of almost all forms of nondegradable toxins based on sunlight irradiation has been widely illustrated.[8,9] A 2-D material, namely, graphitic carbon nitride, with a general abbreviation (g-C_3N_4), represents a good example of a heterogeneous photocatalyst that gains much more treatment decontamination development worldwide in the past two decades. The g-C_3N_4 nanomaterial has been found for more than a decade and utilized mainly to produce H_2 through photocatalytic activity. It has also been globally studied over an extremely wider number of applications in a variety of fields. These include organic pollutant degradation, NO oxidation, catalyst support, CO_2 reduction, solar cells, synthetic organic reactions, etc.[6,10] g-C_3N_4 is also classified as a metal-free-type semiconductor. It absorbs a considerable section of visible range due to its reasonable band gap value (2.7 eV).[6,11] In addition to a huge number of insoluble properties in water and other common solvents, this is mainly referring to the interaction between graphitic layers via van der Waals forces. It is also showing higher stability in both acidic and basic media with increasing temperature until 600 °C.[12,13] Moreover, g-C_3N_4 carries a polymer-like structure that assists in generating vigorous, active radicals through the diversified electron excitation. g-C_3N_4 can

Received: February 7, 2021
Accepted: March 9, 2021
Published: March 17, 2021

ACS Publications

© 2021 The Authors. Published by American Chemical Society

https://doi.org/10.1021/acsomega.1c00697
ACS Omega 2021, 6, 8717–8725

also dynamically reduce oxygen to a superoxide radical in the $O_2^{\cdot-}$ form due to its powerful reduction capability (−1.13 eV versus NHE). On the other hand, some disadvantages are also found in the g-C_3N_4 nanomaterial, which is also faced by individual photocatalysts, including high reincorporation of photoinduced charges, inadequate light response, and low surface area.[14−17] Hence, the researchers think of improving those drawbacks via the possible coupling with any other semiconductor that can possess narrow band gap energy in the form of surface amendment.[16,18] For this purpose, as fundamentally known, the surface area increases while increasing the porous surface in the form known as a porous material. Thus, this is responsible for increasing the active substrate sites for adsorption probability. Mesoporous silica is included in a large number of methods, which are indicated as templates for the fabrication of the porous structure and treatment of acid to boost the generation of pores via ammonia gas loss.[19,20] But such a way fetches a higher toxic prospect in addition to its uncomfortable procedures.[21] A quite good way to generate a porous and large-surface-area material through a thermal method classified as a facile route to yield g-C_3N_4 was proposed by Wang et al. in 2009. The synthesized material was able to absorb visible light easily and effectively decompose Rhodamine B using a photocatalytic process.[10] An ultrathin g-C_3N_4 was prepared by Kadi et al. using thermal treatment of bulk g-C_3N_4 for 6 h as a long-time procedure. Kadi et al. evidenced that this expansion provides a higher-surface-area material and shows a 22-fold increase in the production of H_2 in comparison to the use of the commercial one.[22] Apart from using g-C_3N_4 nanomaterials, bismuth-containing materials might also be utilized as eco-friendly materials for environmental curing. Photocatalysts containing AB_2O_4 spinel oxides also have a polarization effect and crystal facet, which lowers the electron−hole reincorporation in the photocatalytic reaction.[23−25] Recently, Wang et al. showed a noticeable improvement in the CO_2 reduction activity, activated functional groups, and local photogenerated charge carrier separation centers via preparation of $MnCo_2O_4$ microspheres.[24] In this regard, the produced electrons and holes were able to join as an attachment to diverse charges due to the surface polarization, driving the separation of the electron−hole pairs.[26,27] $MnCo_2O_4$ is easily coupled to any other nanomaterial such as g-C_3N_4 via composite formation due to the difference of their band gap edge levels. A proper route of photogenerated charge carriers has been supplied via different band gap energies.[28−37] $MnCo_2O_4$ has a band energy gap of ∼1.7 eV.[30,31] Tetracycline and hexavalent chromium have been felicitously decomposed by CoO@$MnCo_2O_4$ based on visible lighting.[38] Coming from the great behavior of porous $MnCo_2O_4$ and g-C_3N_4, herein, we synthesized mesoporous $MnCo_2O_4$@g-C_3N_4 nanocomposites. The enhanced performance of mesoporous $MnCo_2O_4$@g-C_3N_4 nanocomposites for the hydrogen production process was evaluated. As above, the mesoporous $MnCo_2O_4$ and g-C_3N_4 showed similar performances, cooperation, and quite an increase in the efficiency of photocatalytic activity that may be credited to the less carrier recombination besides the wider absorption range of visible light. The previous methods for the preparation of $MnCo_2O_4$@g-C_3N_4 produced a small surface area.[39] However, in our study, a simple method was used to produce a high surface area of $MnCo_2O_4$@g-C_3N_4 mesoporous photocatalysts for the promoted hydrogen generation.

2. EXPERIMENTAL SECTION

2.1. Materials. EO106-PO70-EO106 (F127), with an average molecule weight of 12,600 g·mol^{-1}, was used as a surfactant. Hydrochloric acid, ethanol, CH_3COOH, Co-$(NO_3)_2{\cdot}6H_2O$, urea manganese acetate, and dicyandiamide were taken from Sigma-Aldrich. A Millipore Milli-Q system was used to purify water.

2.2. Mesoporous $MnCo_2O_4$ Preparation. A sol−gel procedure was used to prepare the mesoporous $MnCo_2O_4$ nanoparticles. F127 was also used as a structure-directing agent tri-block copolymer. The desired product was synthesized by the required 1:0.02:50:2.25:3.75 molar ratios attributed to $MnCo_2O_4$ /F127/C_2H_5OH/HCl/CH_3COOH. In a general procedure, under constant stirring for 60 min, F127 (1.6 g) was added to a solution of ethanol (30 mL). After that, 0.74 mL of HCl and 2.3 mL of CH_3COOH were further added to the previous solution under the same constant magnetic stirring for an extra 30 min. Then, $Co(NO_3)_2{\cdot}6H_2O$ and manganese acetate were considered as the precursors for $MnCo_2O_4$. Hence, 0.0125 mol of cobalt nitrate and 0.0075 mol of manganese acetate were added to the previous mesophase of F127-CH_3COOH to obtain mesoporous $MnCo_2O_4$ after 60 min vigorous stirring, to eliminate ethanol, and to get the required gel. The gel was transferred to a chamber with 40% humidity and temperature up to 40 °C for 12 h. Later, the aging process was carried out at 65 °C for 24 h for that gel, followed by the calcination process, which was carried out in air for 4 h at 550 °C. Throughout this process, a 1 °C/min heating rate and 2 °C/min cooling rates were observed to slip off the surfactant and to obtain the final product as mesoporous $MnCo_2O_4$.

2.3. Preparation of g-C_3N_4. High mesoporous silica (HMS) has a high surface area (ca. 500−1000 m^2·g^{-1}) to realize the similar surface texture of g-C_3N_4. Also, utilize the pyrolysis process of urea and dicyandiamide in air. The preparation of HMS was easily obtained, as reported in the literature.[2] About 50 mL of pure water was ultrasonicated for 30 min in the presence of 1 g of HMS. A mixture of 3 g of dicyandiamide and 5 g of urea was further added. Then, a continuous instigation at 80 °C was carried out to enhance the dissolving process of both components pending complete dissolution. Drying overnight at around 80 °C was applied to take off the extra water amount. Calcination procedures were also performed over 4 h at 550 °C. In the end, the materials obtained were immersed in NH_4HF_2 solution (50 mL, 2 M) with strong stirring up for 24 h to drive out the HMS solid pattern. To release any contaminants adsorbed over the produced g-C_3N_4 nanoparticles, they are easily cleaned by washing several times with water. After that, the synthesized pure material was heated by drying up to 100 °C for 12 h.

2.4. Mesoporous $MnCo_2O_4$@g-C_3N_4 Nanocomposite Synthesis. A water exfoliation process was used to synthesize the desired $MnCo_2O_4$@g-C_3N_4 photocatalysts as follows: 0.2 g of the previously synthesized g-C_3N_4 mixed with mesoporous $MnCo_2O_4$ of a certain amount in deionized water (400 mL). The mixture was dispersed using sonication of a power of 40 kHz for 3 h until thin layered $MnCo_2O_4$@g-C_3N_4 materials were obtained. The final products were specified as *x* $MnCo_2O_4$@g-C_3N_4 and formed by centrifugation. The molar content of $MnCo_2O_4$ in $MnCo_2O_4$@g-C_3N_4 was represented by "*x*" (*x* = 0.5, 1.0, 1.5, and 2.0 wt %).

https://doi.org/10.1021/acsomega.1c00697
ACS Omega 2021, 6, 8717−8725

2.5. Characterizations. The crystalline structures for the produced photocatalysts were measured using a Bruker AXS D4 X-ray diffractogram using Cu Kα radiation. A JEOL JEM-2100F electron microscope, Japan, was used to determine the morphology of the photocatalysts. The FT-IR spectra of the obtained photocatalysts were determined using a PerkinElmer instrument using the KBr technique. A Zahner Zennium electrochemical workstation was used for measuring the photocurrent response of the produced photocatalysts. The surface area of the prepared photocatalysts was examined using a Quantachrome Autosorb instrument. An RF-5301 spectrofluorophotometer, SHIMADZU, Japan, was utilized for examining the photoluminescence spectra of prepared photocatalysts. The V-570 spectrophotometer of Jasco, Japan, was used to determine the band gap energy of the prepared photocatalyst.

2.6. Photocatalytic Tests. A 0.250 L reactor of Pyrex having a window cell and flow system was used to examine the efficiency of $MnCo_2O_4$@g-C_3N_4 photocatalysts or sometimes named as photocatalytic efficiency against H_2 emergence with constant magnetic stirring. A certain amount of photocatalyst was added in the presence of an aqueous solution of 10 vol % glycerol (200 mL). Before the photocatalytic process, Ar gas flow was sanitized for 0.25 h to overcome the water's oxygen. A photoreactor-based 500 W xenon lamp (vertically fixed) in the presence of a UV cutoff screen (λ > 420 nm) was used. The photocatalytic H_2 emergence process started by turning the lamp to an on-position. An interval time was used to measure H_2 evolution throughout the photocatalytic reaction using an Agilent GC 7890A system gas chromatograph instrument.

3. RESULTS AND DISCUSSION

3.1. Depiction of the Materials Obtained. The XRD diffractograms displayed all the expected peaks of g-C_3N_4 and $MnCo_2O_4$@g-C_3N_4 at different $MnCo_2O_4$ contents and were measured as shown in Figure 1A. XRD patterns of pure $MnCo_2O_4$ are shown in Figure 1B. The XRD pattern noted as A represents the original peak of the typical g-C_3N_4 phase existing at 27.4° (JCPDS no. 87-1526), evidencing a diffraction plane indexed as (002) together with 0.325 nm *d*-spacing.[3,4] In $MnCo_2O_4$@g-C_3N_4 samples, there are no observable peaks for $MnCo_2O_4$, which may be credited to the high dispersion of small-sized $MnCo_2O_4$ on the surface of g-C_3N_4 or may be due to the lower detection limit of $MnCo_2O_4$ determined by the XRD instrument. Also, we noticed that the addition of $MnCo_2O_4$ to g-C_3N_4 leads to reduced g-C_3N_4 peak intensity. The pattern denoted as B reveals that all XRD peaks are referred to spinal $MnCo_2O_4$ (JCPDS no. 01-1130), as illustrated in Figure 1B.[39]

The FT-IR spectra of parent g-C_3N_4 and 1.5 and 2.0 wt % $MnCo_2O_4$@g-C_3N_4 nanocomposites are illustrated in Figure 2. A peak at 807 cm^{-1}, referring to the triazine unit stretching mode in pure g-C_3N_4 nanosheets, was observed.[40,41] However, a small turn at 807 cm^{-1} for 1.5 and 2.0 wt % $MnCo_2O_4$@g-C_3N_4 nanocomposites has been observed, indicating a strong coupling between $MnCo_2O_4$@g-C_3N_4 nanoparticles and the g-C_3N_4 nanosheet.[39] It is seen from the FT-IR spectra that the peak intensity is worthily reduced with the content increase of $MnCo_2O_4$. Peaks at 1639, 1575, 1439, 1325, and 1250 cm^{-1} are designated to the CN-heterocyclic stretching mode.[42−44] Also, another broad peak suggesting the stretching vibration of the N−H group is mentioned in the range of 3500−3000 cm^{-1}.[45] Moreover, after $MnCo_2O_4$ nanoparticle incorporation with g-C_3N_4, there is an apparent confirmation that all the examined peaks are not shifted.

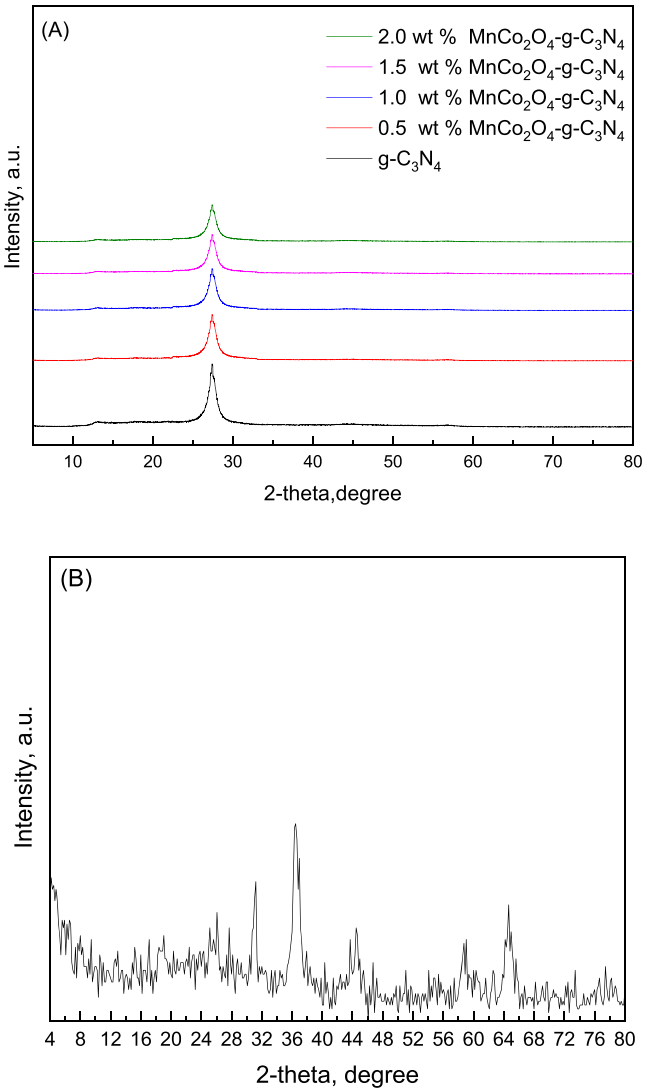

Figure 1. XRD patterns of g-C_3N_4 and $MnCo_2O_4$@g-C_3N_4 samples (A) and XRD pattern of $MnCo_2O_4$ sample (B).

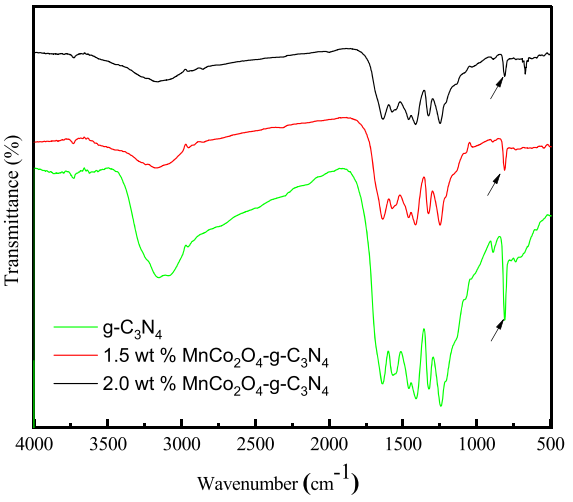

Figure 2. FT-IR spectra analysis of produced g-C_3N_4 photocatalysts compared to 1.5 and 2.0 wt % $MnCo_2O_4$@g-C_3N_4 samples.

https://doi.org/10.1021/acsomega.1c00697
ACS Omega 2021, 6, 8717−8725

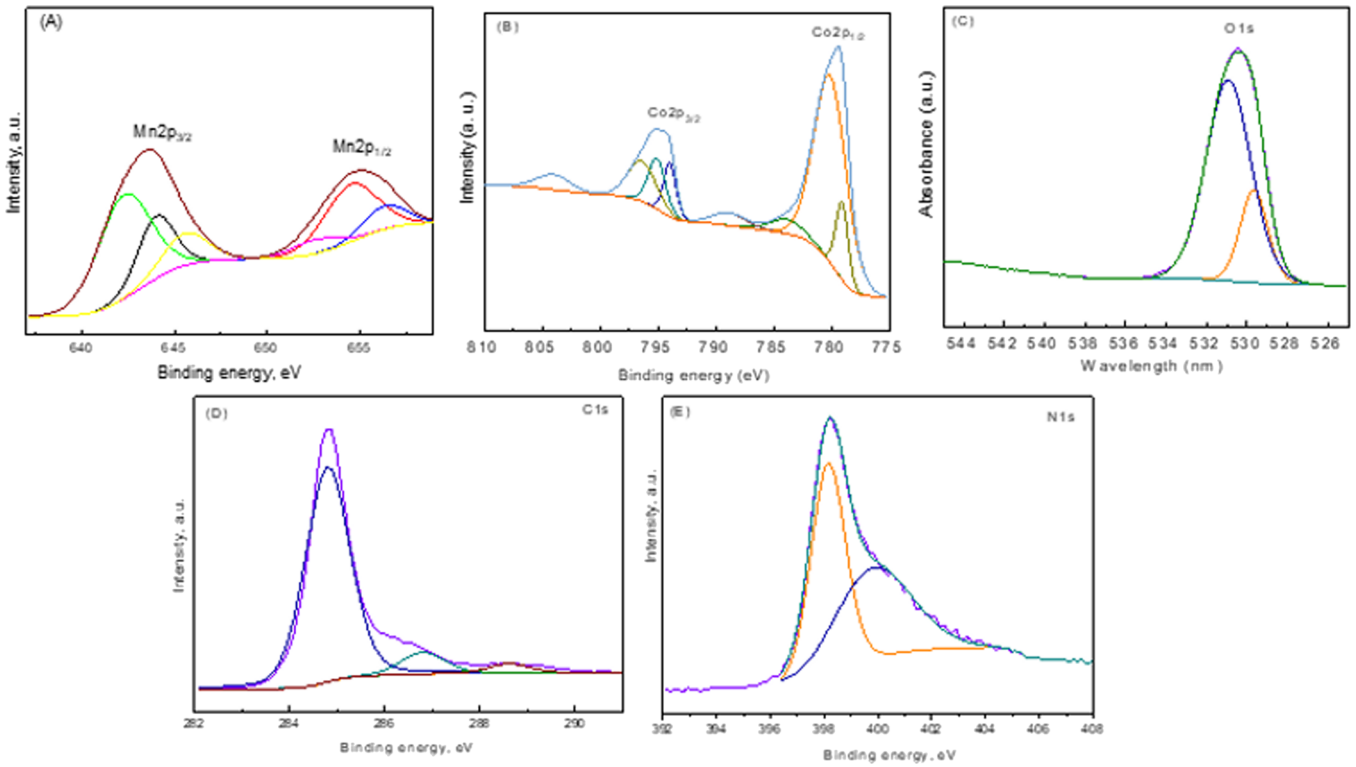

Figure 3. High-resolution XPS of 1.5 wt % $MnCo_2O_4$@g-C_3N_4 nanocomposite showing Mn2p (A), Co2p (B), O1s (C), C1s (D), and N1s (E).

Figure 3 displays the XPS spectra for the desired 1.5 wt % $MnCo_2O_4$@g-C_3N_4 products. Three peaks at ∼642.4, 644.1, and 645.6 eV and ∼652.3, 654.5, and 656.5 eV for $Mn2p_{3/2}$ and $Mn2p_{1/2}$ are observed correspondingly, as seen in Figure 3A, emphasizing the presence of Mn^{2+}, Mn^{3+}, and Mn^{4+} ions in $MnCo_2O_4$.[39] Two peaks at ∼779.1 and 780.2 eV and ∼796.2 and 791.1 eV for $Co2p_{3/2}$ and $Co2p_{1/2}$ are observed correspondingly, as seen in Figure 3B, emphasizing the presence of Co^{2+} and Co^{3+} ions in $MnCo_2O_4$.[39] Two peaks at ∼529.6 and 530.8 eV for O1s are observed, as displayed in Figure 3C, emphasizing the existence of oxygen ions in $MnCo_2O_4$.[39,46] Peaks at ∼287.9 and ∼284.6 eV are two essential peaks depicted in Figure 3D, which are due to the hybridized sp^2 carbon enlisted to nitrogen near the C−C bonds in the aromatic structure.[47,48] The sp^2 hybridization (pyridine carbon) is shown in (Figure 3D). The peak at 398.3 eV is due to the sp^2 hybridization of the nitrogen atom. Mostly, the graphite-like C_3N_4 structure is created by the observation of all the peaks mentioned above.[49,50]

Figure 4A displays the TEM observation of $MnCo_2O_4$ nanoparticles. The images indicate that the nanoparticles are symmetric and have average particle sizes of 8−10 nm. Figure 4B depicts the TEM images of g-C_3N_4, which show a clear graphene-resembling sheet structure as an apparent confirmation for the formation of the g-C_3N_4 nanosheet. In the 1.5 wt % $MnCo_2O_4$@g-C_3N_4 nanocomposites, TEM images show that $MnCo_2O_4$ nanoparticles are distributed uniformly onto the g-C_3N_4 nanosheet as seen in Figure 3C. The less agglomerated $MnCo_2O_4$ nanoparticles also have a size of 10−15 nm and keep the spherical shape. Figure 4D displays the 1.5 wt % $MnCo_2O_4$@g-C_3N_4 HR-TEM picture. The lattice planes of g-C_3N_4 (002) and $MnCo_2O_4$ (111) with 0.320 and 0.479 nm lattice spacing are observed, respectively, as shown in Figure 4D,[39] which confirm $MnCo_2O_4$ and g-C_3N_4 heterojunction formation.

The N_2 adsorption−desorption isotherms of parent $MnCo_2O_4$, g-C_3N_4, and the 1.5 wt % $MnCo_2O_4$@g-C_3N_4 nanocomposite are depicted in Figure 5. The produced materials show mesoporous characteristics, which are mainly estimated by the H3 hysteresis at 0.62−0.88 virtual pressure, as shown in the type IV isotherms. Such results support the formation of porous, clear structures.[51,52] The porous feature of g-C_3N_4 was preserved even after $MnCo_2O_4$ was distributed onto the g-C_3N_4 skim. The surface area values for pure $MnCo_2O_4$ and g-C_3N_4 are 240 and 175 m^2/g, respectively. After $MnCo_2O_4$ incorporation with g-C_3N_4, the surface areas of 0.5, 1.0, 1.5, and 2.0 wt % $MnCo_2O_4$@g-C_3N_4 nanocomposites are 192, 203, 205, and 208 m^2/g, respectively, as displayed in Table 1. The produced photocatalysts provide a highly efficient photocatalytic process through their obtained higher surface area. Moreover, the diffusion/mass transit is highly supported by the observed mesostructures, which also encourages the presence of light inside the pores that boosts the efficiency of solar energy.

The spectra of UV−Vis for parent $MnCo_2O_4$, g-C_3N_4, and $MnCo_2O_4$@g-C_3N_4 heterojunctions are presented in Figure 6. The absorption range of the obtained $MnCo_2O_4$@g-C_3N_4 photocatalysts is visibly increased through the supplement of $MnCo_2O_4$ to the g-C_3N_4 sheets. An apparent movement for the g-C_3N_4 nanosheet absorption edge toward the blue region is mentioned, emulated to the $MnCo_2O_4$@g-C_3N_4 nanocomposites at variable $MnCo_2O_4$ contents as listed in Table 2. The 1.5 and 2.0 wt % $MnCo_2O_4$@g-C_3N_4 nanocomposites exhibit the smallest band gap energies (∼1.99 eV) that allow the minimum energy to get the extreme efficient electron transfer compared to pure $MnCo_2O_4$ or g-C_3N_4 (1.70 and 2.70 eV, respectively). Thus, the higher content of $MnCo_2O_4$

https://doi.org/10.1021/acsomega.1c00697
ACS Omega 2021, 6, 8717−8725

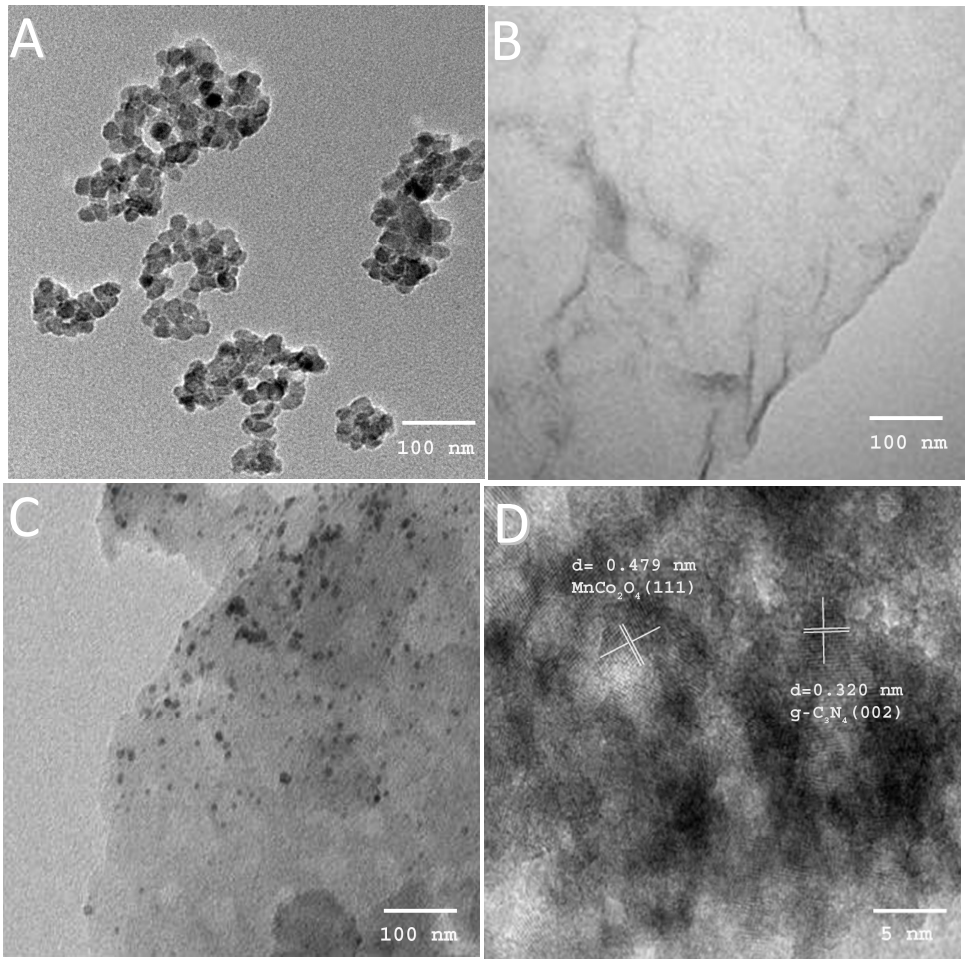

Figure 4. TEM image of $MnCo_2O_4$ (A), g-C_3N_4 (B), and 1.5 wt % $MnCo_2O_4$@g-C_3N_4 (C) samples and HRTEM image of 1.5 wt % $MnCo_2O_4$@g-C_3N_4 (D) sample.

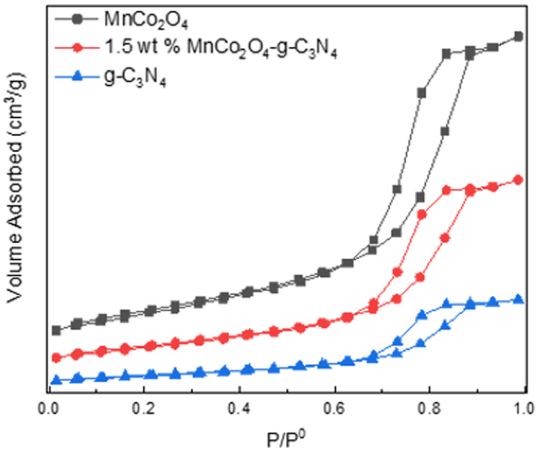

Figure 5. Nitrogen adsorption−desorption isotherms of pure $MnCo_2O_4$, pure g-C_3N_4, and 1.5 wt % $MnCo_2O_4$@g-C_3N_4 nanocomposites.

incorporated onto g-C_3N_4 resulted in the minimum band gap value of the produced $MnCo_2O_4$@g-C_3N_4 nanocomposites.[53,54]

3.2. The Examination of H_2 Progression. The molecular H_2 generation experimentations were examined in the presence of pure $MnCo_2O_4$ nanoparticles, pure g-C_3N_4, and the heterojunctions of $MnCo_2O_4$@g-C_3N_4 nanocomposites at

Table 1. BET Surface Area of g-C_3N_4 and $MnCo_2O_4$@g-C_3N_4 Samples

sample	S_{BET} (m^2/g)
g-C_3N_4	175.00
0.5 wt % $MnCo_2O_4$@g-C_3N_4	192.00
1.0 wt % $MnCo_2O_4$@g-C_3N_4	203.00
1.5 wt % $MnCo_2O_4$@g-C_3N_4	205.00
2.0 wt % $MnCo_2O_4$@g-C_3N_4	208.00
$MnCo_2O_4$	240.00

various $MnCo_2O_4$ contents (0.5−2.0 wt %) together with glycerol (10 vol %) as a hole scrounger. The experiments confirm that there is no H_2 generation observed without using the photocatalyst or in the dark. Figure 7A displays the molecular H_2 production versus overall time course above photocatalysts. A noticeable H_2 evolution activity is observed in the parent $MnCo_2O_4$ and g-C_3N_4 under visible lighting at room temperature for 9 h (nearly 972 and 400 $\mu mol \cdot g^{-1} \cdot h^{-1}$). This is ascribed to the quick charge carrier's reincorporation, remarking that parent photocatalysts are both not efficient for photocatalytic H_2 production.[55] The data show that the variable amounts of $MnCo_2O_4$ onto g-C_3N_4 possess a considerable impact on H_2 production. The production of H_2 is highly raised by raising the $MnCo_2O_4$ contents by 1.5 wt %. The H_2 value is highly increased and reaches a maximum of 15,660 $\mu mol \cdot g^{-1} \cdot h^{-1}$ in the presence of a 1.5 wt % $MnCo_2O_4$@

https://doi.org/10.1021/acsomega.1c00697
ACS Omega 2021, 6, 8717−8725

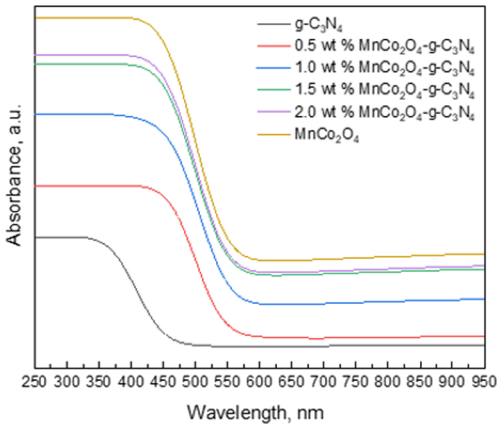

Figure 6. UV−Vis spectra of pure $MnCo_2O_4$, g-C_3N_4, and different $MnCo_2O_4$@g-C_3N_4 samples.

Table 2. Band Gap of $MnCo_2O_4$, g-C_3N_4, and $MnCo_2O_4$@g-C_3N_4 Samples

sample	band gap (eV)
g-C_3N_4	2.70
0.5 wt % $MnCo_2O_4$@g-C_3N_4	2.24
1.0 wt % $MnCo_2O_4$@g-C_3N_4	2.12
1.5 wt % $MnCo_2O_4$@g-C_3N_4	1.99
2.0 wt % $MnCo_2O_4$@g-C_3N_4	1.96
$MnCo_2O_4$	1.70

g-C_3N_4 nanocomposite. The adjustable content of $MnCo_2O_4$ nanoparticles, together with high dispersion on the g-C_3N_4 surface, plays a significant role in getting such an explanation. This agrees with the TEM images (Figure 4C), in which the hole−electron pair separation is highly associated.[56] The primary principles for producing the H_2 process using the $MnCo_2O_4$@g-C_3N_4 nanocomposite refer to four main factors, including crystallinity, band gap tightening, crystallite sizes, and large surface area. Figure 7B exhibits the impact of the 1.5 wt % $MnCo_2O_4$@g-C_3N_4 photocatalyst dose on H_2 yield, which enhances to 10,550, 12,150, 15,660, 19,755, and 21,870 μmol·g^{-1}·h^{-1} with increasing photocatalyst content from 0.5 to 2.5 g/L. Such results are due to the number of active sites on the 1.5 wt % $MnCo_2O_4$@g-C_3N_4 surface, which is increased. The higher content from the photocatalyst resulted in the decrease in H_2 yield (more than 2.5 g/L reduces the yield to 18,144 μmol·g^{-1}·h^{-1}). This has resulted from the reduction in the light infiltration through the photocatalyst surface as the particles' number is increased.

To emphasize the obtained data, the PL spectra and PC responses for all produced samples were examined, as displayed in Figure 8. The findings of the PL spectra exhibit that high emission intensity is observed in g-C_3N_4. However, a measured reduction in the intensity, and a redshift of peak position, is detected with increasing $MnCo_2O_4$ content into the g-C_3N_4 sheet in the following order: g-C_3N_4 > $MnCo_2O_4$ > 0.5 wt % $MnCo_2O_4$@g-C_3N_4 > 1.0 wt % $MnCo_2O_4$@g-C_3N_4 > 1.5 wt % $MnCo_2O_4$@g-C_3N_4 > 2.0 wt % $MnCo_2O_4$@g-C_3N_4. Pure $MnCo_2O_4$ and g-C_3N_4 show higher PL intensities, which may be investigated by hastening the reincorporation rate of holes and electrons, and this might give rise to a noticeable decrease in the H_2 yield. Moreover, the PL intensity is reduced as $MnCo_2O_4$ nanoparticles are introduced onto the g-C_3N_4 sheet. Such behavior resulted from the delay in the charge

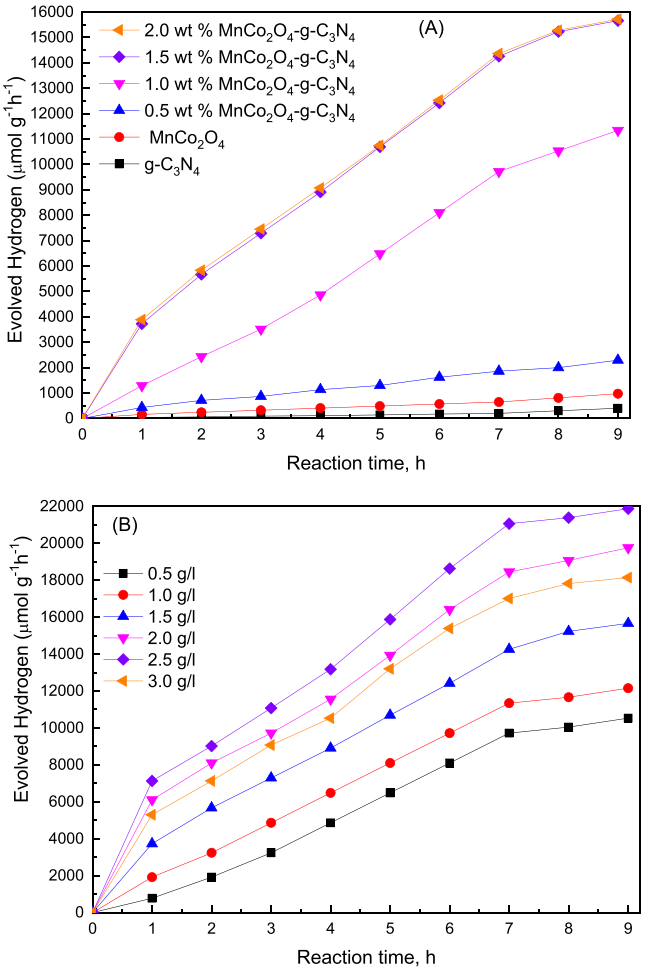

Figure 7. Hydrogen generation using the produced photocatalysts (A). Impact of the dose of the optimized 1.5 wt % $MnCo_2O_4$@g-C_3N_4 nanocomposite (B).

carrier's reincorporation rate, which created a high H_2 yield. The transient photocurrent responses for all produced photocatalysts are illustrated in Figure 8B. Depending upon the results, it is clearly mentioned that all nanocomposites have high photocurrent densities and the values are noticeably raised with increasing $MnCo_2O_4$ contents as follows: g-C_3N_4 < $MnCo_2O_4$ < 0.5 wt % $MnCo_2O_4$@g-C_3N_4 < 1.0 wt % $MnCo_2O_4$@g-C_3N_4 < 1.5 wt % $MnCo_2O_4$@g-C_3N_4 < 2.0 wt % $MnCo_2O_4$@g-C_3N_4. PC and PL data for the 1.5 wt % $MnCo_2O_4$@g-C_3N_4 nanocomposite exhibit reduced PL values and elevate the photocurrent compared with pure g-C_3N_4. Such findings totally confirm the results mentioned above. The fundamental stumbling block of hastening the rate of reincorporation for holes and photons/electrons in pure g-C_3N_4 has been completely barred through the production of $MnCo_2O_4$@g-C_3N_4 nanocomposites and wonderfully enhances the photocatalytic efficiency. These measurements have supported the demonstration based on the increase in the photocatalytic rendering joint with the charge carrier reincorporation rate reduction. The most important key agents in this process are based on the photocatalyst stability and durability and the major directions of its workable recyclability. The steadiness of the produced 1.5 wt % $MnCo_2O_4$@g-C_3N_4 nanocomposite has been examined by reusing the photocatalyst five times in the production of H_2 photocatalytic

https://doi.org/10.1021/acsomega.1c00697
ACS Omega 2021, 6, 8717−8725

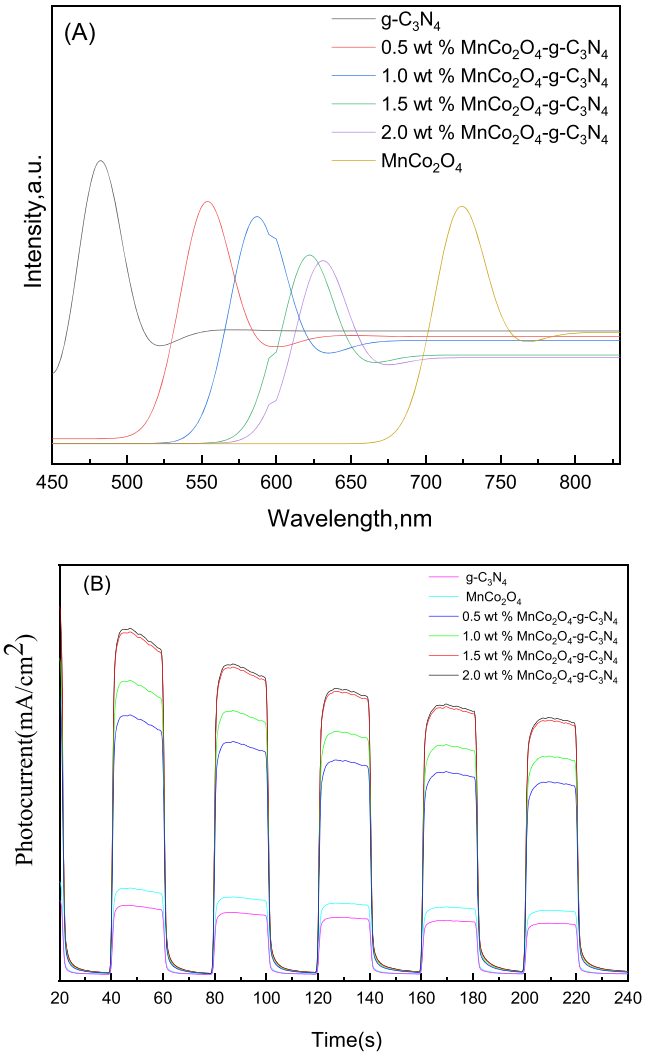

Figure 8. PL spectra (A) and transient photocurrent measurements (B) of pure $MnCo_2O_4$, g-C_3N_4, and varied $MnCo_2O_4$@g-C_3N_4 photocatalysts.

activity, as presented in Figure 9. The data also specified no conspicuous reduction in the photocatalytic H_2 evolution activity for the produced material. Visible light illumination is exposed to five times cycles as the maximum number of cycles, and such an effect proposes that the 1.5 wt % $MnCo_2O_4$@g-C_3N_4 nanocomposite demonstrates high stability through visible lighting. The most common notified empirical equations for determining both valence and conduction band positions of photocatalysts are shown below, as the literature illustrates.[57]

$$E_{CB} = X - E^e - 0.5E_g \quad (1)$$

$$E_{VB} = E_{CB} + E_g \quad (2)$$

The band gap values of both pure $MnCo_2O_4$ and g-C_3N_4 are presented as E_g, while E^e is the hydrogen scale-free electron energy equal to 4.5 eV. The electronegativity of pure $MnCo_2O_4$ nanoparticles and g-C_3N_4 is presented as X, and the values are 4.77 and 4.72 eV, respectively. The conduction band positions of pure $MnCo_2O_4$ nanoparticles and the g-C_3N_4 sheet acquired from eqs 1 and 2 are −0.58 and −1.13 eV, respectively. The valence bands of $MnCo_2O_4$ nanoparticles and

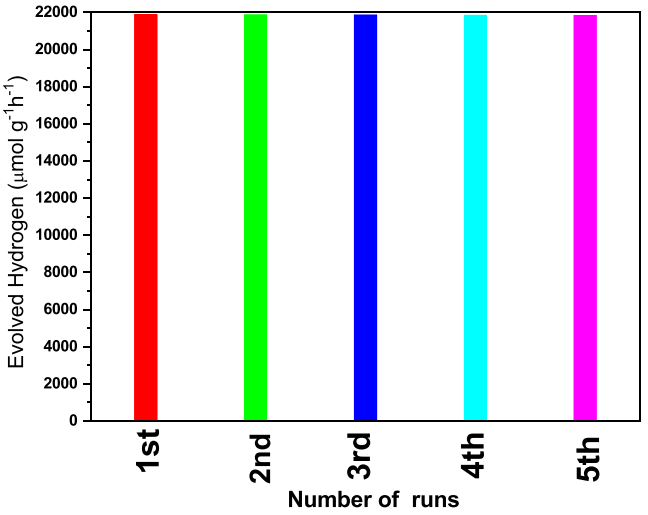

Figure 9. Impact of the 1.5 wt % $MnCo_2O_4$@g-C_3N_4 photocatalyst on the hydrogen production, showing the stability for five consecutive runs.

g-C_3N_4 sheets amount to +1.12 and +1.57 eV, respectively. The attained values of valence bands and conduction bands acquired a display that the expected mechanism for the production of H_2 in the presence of the $MnCo_2O_4$@g-C_3N_4 nanocomposite supports a heterojunction as the literature illustrates, as shown in Scheme 1.[58] In such a scheme, as the

Scheme 1. Photocatalytic Process of 1.5 wt % $MnCo_2O_4$@g-C_3N_4 Photocatalyst for Hydrogen Production

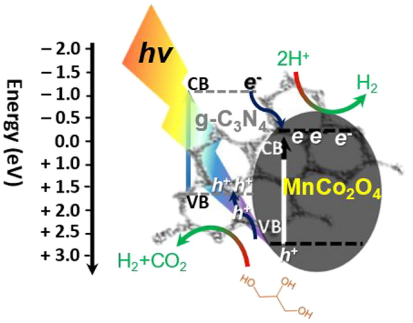

$MnCo_2O_4$@g-C_3N_4 surfaces are attacked by the photons, a wide range of visible light is collected by g-C_3N_4, followed by a logical excitation for the electrons to the conduction band from its valence band, which consequently move to the $MnCo_2O_4$ conduction band for H_2 formation through the reduction of H^+. Therefore, the photogenerated holes departed in the g-C_3N_4 valence band consumed for the glycerol oxidation, as illustrated in Scheme 1. Such a process led to the segregation of photogenerated electrons and holes; hence, the reincorporation rate turns relatively weak.

4. CONCLUSIONS

In summary, a sol−gel technique has been applied to prepare $MnCo_2O_4$, g-C_3N_4, and $MnCo_2O_4$@g-C_3N_4 nanocomposites at variable $MnCo_2O_4$ amounts for promoting H_2 production. XRD shows the successful formation of $MnCo_2O_4$ that is integrated onto the g-C_3N_4. The $MnCo_2O_4$ nanoparticles show 8 nm spherical shapes from TEM images. The nanoparticles are also spread uniformly inside the g-C_3N_4 nanosheet. The

https://doi.org/10.1021/acsomega.1c00697
ACS Omega 2021, 6, 8717−8725

surface-active sites, as well as the light gathering, are significantly increased by the $MnCo_2O_4$ nanoparticles. The $MnCo_2O_4$@g-C_3N_4 nanocomposites show a significant increase in the H_2 evolution yields about ∼55 and 23 times than those observed for g-C_3N_4 and neat $MnCo_2O_4$, respectively. The confirmed increase in the photocatalytic efficiency regarding its H_2 production is mainly emphasized by a narrow band gap, better charge carrier separation, and more surface-active sites. An insignificant decrease in the photocatalytic competence for the optimized $MnCo_2O_4$@g-C_3N_4 photocatalyst has been observed after five times photocatalytic cycles. Such observation enhances the higher probability of its stability and durability via the visible lighting process.

AUTHOR INFORMATION

Corresponding Author

Reda M. Mohamed − *Department of Chemistry, Faculty of Science, King Abdulaziz University, Jeddah 21589, Kingdom of Saudi Arabia; Advanced Materials Department, Central Metallurgical R&D Institute (CMRDI), Helwan, Cairo 11421, Egypt;* orcid.org/0000-0002-6182-6880; Email: redama123@yahoo.com

Authors

Maha Alhaddad − *Department of Chemistry, Faculty of Science, King Abdulaziz University, Jeddah 21589, Kingdom of Saudi Arabia*

Mohamed H. H. Mahmoud − *Department of Chemistry, College of Science, Taif University, Taif 21944, Saudi Arabia*

Complete contact information is available at: https://pubs.acs.org/10.1021/acsomega.1c00697

Notes

The authors declare no competing financial interest.

ACKNOWLEDGMENTS

The authors would like to thank Taif University Researchers Supporting Project (number TURSP-2020/158), Taif University, Taif, Saudi Arabia, for supporting this work.

REFERENCES

(1) Shawky, A.; Mohamed, R. M.; Mkhalid, I. A.; Youssef, M. A.; Awwad, N. S. Visible light-responsive Ag/$LaTiO_3$ nanowire photocatalysts for efficient elimination of atrazine herbicide in water. *J. Mol. Liq.* **2020**, *299*, 112163.

(2) Mohamed, R. M.; Aazam, E. S. Characterization and catalytic properties of nano-sized Au metal catalyst on titanium containing high mesoporous silica (Ti-HMS) synthesized by photo-assisted deposition and impregnation methods. *Int. J. Photoenergy* **2011**, *2011*, 1.

(3) Mohamed, R. M. Synthesis and characterization of AgCl@ graphitic carbon nitride hybrid materials for the photocatalytic degradation of atrazine. *Ceram. Int.* **2015**, *41*, 1197−1204.

(4) Dong, F.; Li, Y.; Wang, Z.; Ho, W.-K. Enhanced visible light photocatalytic activity and oxidation ability of porous graphene-like g-C3N4 nanosheets via thermal exfoliation. *Appl. Surf. Sci.* **2015**, *358*, 393−403.

(5) Mohamed, R. M.; Aazam, E. S. Preparation and characterization of core−shell polyaniline/mesoporous Cu_2O nanocomposites for the photocatalytic oxidation of thiophene. *Appl. Surf. Sci.* **2014**, *480*, 100−107.

(6) Mamba, G.; Mishra, A. K. Graphitic carbon nitride (g-C_3N_4) nanocomposites: a new and exciting generation of visible light driven photocatalysts for environmental pollution remediation. *Appl. Catal., B* **2016**, *198*, 347−377.

(7) Rashid, J.; Barakat, M. A.; Mohamed, R. M.; Ibrahim, I. A. Enhancement of photocatalytic activity of zinc/cobalt spinel oxides by doping with ZrO_2 for visible light photocatalytic degradation of 2-chlorophenol in wastewater. *J. Photochem. Photobiol., A* **2014**, *284*, 1−7.

(8) Mohamed, R. M.; Harraz, F. A.; Mkhalid, I. A. Hydrothermal synthesis of size-controllable Yttrium Orthovanadate (YVO_4) nanoparticles and its application in photocatalytic degradation of direct blue dye. *J. Alloys Compd.* **2012**, *532*, 55−60.

(9) Mohamed, R. M.; Mkhalid, I. A.; Shawky, A. Facile synthesis of Pt−In_2O_3/$BiVO_4$ nanospheres with improved visible-light photocatalytic activity. *J. Alloys Compd.* **2019**, *775*, 542−548.

(10) Wang, X.; Maeda, K.; Thomas, A.; Takanabe, K.; Xin, G.; Carlsson, J. M.; Domen, K.; Antonietti, M. A metal-free polymeric photocatalyst for hydrogen production from water under visible light. *Nat. Mater.* **2009**, *8*, 76−80.

(11) Mohamed, R. M.; Mkhalid, I. A. Visible light photocatalytic degradation of cyanide using Au−TiO_2/multi-walled carbon nanotube nanocomposites. *J. Ind. Eng. Chem.* **2015**, *22*, 390−395.

(12) Ismail, A. A.; Ibrahim, I. A.; Mohamed, R. M. Sol−gel synthesis of vanadia−silica for photocatalytic degradation of cyanide. *Appl. Catal., B* **2003**, *45*, 161−166.

(13) Zhao, Z.; Sun, Y.; Dong, F. Graphitic carbon nitride based nanocomposites: a review. *Nanoscale* **2015**, *7*, 15−37.

(14) Zhang, Y.; Schnepp, Z.; Cao, J.; Ouyang, S.; Li, Y.; Ye, J.; Liu, S. Biopolymer-activated graphitic carbon nitride towards a sustainable photocathode material. *Sci. Rep.* **2013**, *3*, 2163.

(15) Wen, P.; Gong, P.; Sun, J.; Wang, J.; Yang, S. Design and synthesis of Ni-MOF/CNT composites and rGO/carbon nitride composites for an asymmetric supercapacitor with high energy and power density. *J. Mater. Chem. A* **2015**, *3*, 13874−13883.

(16) Habibi-Yangjeh, A.; Mousavi, M.; Nakata, K. Boosting visible-light photocatalytic performance of g-C_3N_4/Fe_3O_4 anchored with $CoMoO_4$ nanoparticles: novel magnetically recoverable photocatalysts. *J. Photochem. Photobiol., A* **2019**, *368*, 120−136.

(17) Yu, W.; Chen, J.; Shang, T.; Chen, L.; Gu, L.; Peng, T. Direct Z-scheme g-C_3N_4/WO_3 photocatalyst with atomically defined junction for H_2 production. *Appl. Catal., B* **2017**, *219*, 693−704.

(18) Mohamed, R. M.; McKinney, D.; Kadi, M. W.; Mkhalid, I. A.; Sigmund, W. Platinum/zinc oxide nanoparticles: enhanced photocatalysts degrade malachite green dye under visible light conditions. *Ceram. Int.* **2016**, *42*, 9375−9381.

(19) Groenewolt, M.; Antonietti, M. Synthesis of g-C_3N_4 nanoparticles in mesoporous silica host matrices. *Adv. Mater.* **2005**, *17*, 1789−1792.

(20) Cheng, F.; Wang, H.; Dong, X. The amphoteric properties of g-C_3N_4 nanosheets and fabrication of their relevant heterostructure photocatalysts by an electrostatic re-assembly route. *Chem. Commun.* **2015**, *51*, 7176−7179.

(21) Lv, J.; Dai, K.; Zhang, J.; Liu, Q.; Liang, C.; Zhu, G. Facile constructing novel 2D porous g-C_3N_4/BiOBr hybrid with enhanced visible-light-driven photocatalytic activity. *Sep. Purif. Technol.* **2017**, *178*, 6−17.

(22) Kadi, M. W.; McKinney, D.; Mohamed, R. M.; Mkhalid, I. A.; Sigmund, W. Fluorine doped zinc oxide nanowires: enhanced photocatalysts degrade malachite green dye under visible light conditions. *Ceram. Int.* **2016**, *42*, 4672−4678.

(23) Liu, Z.-Q.; Xu, Q.-Z.; Wang, J.-Y.; Li, N.; Guo, S.-H.; Su, Y.-Z.; Wang, H.-J.; Zhang, J.-H.; Chen, S. Facile hydrothermal synthesis of urchin-like $NiCo_2O_4$ spheres as efficient electrocatalysts for oxygen reduction reaction. *Int. J. Hydrogen Energy* **2013**, *38*, 6657−6662.

(24) Wang, S.; Hou, Y.; Wang, X. Development of a stable $MnCo_2O_4$ cocatalyst for photocatalytic CO_2 reduction with visible light. *ACS Appl. Mater. Interfaces* **2015**, *7*, 4327−4335.

(25) Luo, Z.; Irtem, E.; Ibáñez, M.; Nafria, R.; Martí-Sánchez, S.; Genç, A.; de la Mata, M.; Liu, Y.; Cadavid, D.; Llorca, J.; Arbiol, J.; Andreu, T.; Morante, J. R.; Cabot, A. Mn3O4@ CoMn2O4−CoxOy Nanoparticles: Partial Cation Exchange Synthesis and Electrocatalytic

Properties toward the Oxygen Reduction and Evolution Reactions. *ACS Appl. Mater. Interfaces* **2016**, *8*, 17435−17444.
(26) Kim, J. G.; Lee, S. H.; Kim, Y.; Kim, W. B. Fabrication of free-standing $ZnMn_2O_4$ mesoscale tubular arrays for lithium-ion anodes with highly reversible lithium storage properties. *ACS Appl. Mater. Interfaces* **2013**, *5*, 11321−11328.
(27) Wu, X.; Xiang, Y.; Peng, Q.; Wu, X.; Li, Y.; Tang, F.; Song, R.; Liu, Z.; He, Z.; Wu, X. Green-low-cost rechargeable aqueous zinc-ion batteries using hollow porous spinel $ZnMn_2O_4$ as the cathode material. *J. Mater. Chem. A* **2017**, *5*, 17990−17997.
(28) Mohamed, R. M.; Shawky, A. CNT supported Mn-doped ZnO nanoparticles: simple synthesis and improved photocatalytic activity for degradation of malachite green dye under visible light. *Appl. Nanosci.* **2018**, *8*, 1179−1188.
(29) Jang, J. S.; Kim, H. G.; Lee, J. S. Heterojunction semiconductors: A strategy to develop efficient photocatalytic materials for visible light water splitting. *Catal. Today* **2012**, *185*, 270−277.
(30) Chen, H.; Leng, W.; Xu, Y. Enhanced visible-light photoactivity of $CuWO_4$ through a surface-deposited CuO. *J. Phys. Chem. C* **2014**, *118*, 9982−9989.
(31) Joshi, U. A.; Maggard, P. A. $CuNb_3O_8$: a p-type semiconducting metal oxide photoelectrode. *J. Phys. Chem. Lett.* **2012**, *3*, 1577−1581.
(32) Guo, F.; Shi, W.; Wang, H.; Han, M.; Li, H.; Huang, H.; Liu, Y.; Kang, Z. Facile fabrication of a CoO/g-C_3N_4 p−n heterojunction with enhanced photocatalytic activity and stability for tetracycline degradation under visible light. *Catal. Sci. Technol.* **2017**, *7*, 3325−3331.
(33) Pinaud, B. A.; Chen, Z.; Abram, D. N.; Jaramillo, T. F. Thin films of sodium birnessite-type MnO_2: optical properties, electronic band structure, and solar photoelectrochemistry. *J. Phys. Chem. C* **2011**, *115*, 11830−11838.
(34) Yang, J.; Chen, D.; Zhu, Y.; Zhang, Y.; Zhu, Y. 3D-3D porous Bi_2WO_6/graphene hydrogel composite with excellent synergistic effect of adsorption-enrichment and photocatalytic degradation. *Appl. Catal., B* **2017**, *205*, 228−237.
(35) Wen, X.-J.; Zhang, C.; Niu, C.-G.; Zhang, L.; Zeng, G.-M.; Zhang, X.-G. Highly enhanced visible light photocatalytic activity of CeO_2 through fabricating a novel p−n junction BiOBr/CeO_2. *Catal. Commun.* **2017**, *90*, 51−55.
(36) Nanda, B.; Pradhan, A. C.; Parida, K. M. Fabrication of mesoporous CuO/ZrO_2-MCM-41 nanocomposites for photocatalytic reduction of Cr(VI). *Chem. Eng. J.* **2017**, *316*, 1122−1135.
(37) Lu, D.; Chai, W.; Yang, M.; Fang, P.; Wu, W.; Zhao, B.; Xiong, R.; Wang, H. Visible light induced photocatalytic removal of Cr(VI) over TiO_2-based nanosheets loaded with surface-enriched CoOx nanoparticles and its synergism with phenol oxidation. *Appl. Catal., B* **2016**, *190*, 44−65.
(38) Zheng, J.; Lei, Z. Incorporation of CoO nanoparticles in 3D marigold flower-like hierarchical architecture $MnCo_2O_4$ for highly boosting solar light photo-oxidation and reduction ability. *Appl. Catal., B* **2018**, *237*, 1−8.
(39) Zheng, C.-W.; Niu, H.-Y.; Liang, C.; Niu, C.-G.; Zhao, X.-F.; Zhang, L.; Li, J.-S.; Guo, H.; Liu, H.-Y.; Liang, S. A study on advanced oxidation mechanism of $MnCo_2O_4$/g-C_3N_4 degradation of nitrobenzene: Sacrificial oxidation and radical oxidation. *Chem. Eng. J.* **2021**, *403*, 126400.
(40) He, Y.; Zhang, L.; Teng, B.; Fan, M. New application of Z-scheme Ag_3PO_4/g-C_3N_4 composite in converting CO_2 to fuel. *Environ. Sci. Technol.* **2015**, *49*, 649−656.
(41) Yan, S. C.; Li, Z. S.; Zou, Z. G. Photodegradation performance of g-C_3N_4 fabricated by directly heating melamine. *Langmuir* **2009**, *25*, 10397−10401.
(42) Fu, J.; Tian, Y.; Chang, B.; Xi, F.; Dong, X. BiOBr−carbon nitride heterojunctions: synthesis, enhanced activity and photocatalytic mechanism. *J. Mater. Chem.* **2012**, *22*, 21159−21166.
(43) Huang, S.; Xu, Y.; Xie, M.; Xu, H.; He, M.; Xia, J.; Huang, L.; Li, H. Synthesis of magnetic $CoFe_2O_4$/g-C_3N_4 composite and its enhancement of photocatalytic ability under visible-light. *Colloids Surf., A* **2015**, *478*, 71−80.
(44) Ye, L.; Deng, K.; Xu, F.; Tian, L.; Peng, T.; Zan, L. Increasing visible-light absorption for photocatalysis with black BiOCl. *Phys. Chem. Chem. Phys.* **2012**, *14*, 82−85.
(45) Yao, Y.; Wu, G.; Lu, F.; Wang, S.; Hu, Y.; Zhang, J.; Huang, W.; Wei, F. Enhanced photo-Fenton-like process over Z-scheme $CoFe_2O_4$/g-C_3N_4 heterostructures under natural indoor light. *Environ. Sci. Pollut. Res.* **2016**, *23*, 21833−21845.
(46) Wei, X. Q.; Man, B. Y.; Liu, M.; Xue, C. S.; Zhuang, H. Z.; Yang, C. Blue luminescent centers and microstructural evaluation by XPS and Raman in ZnO thin films annealed in vacuum, N_2 and O_2. *Phys. B* **2007**, *388*, 145−152.
(47) Wang, J.-C.; Yao, H.-C.; Fan, Z.-Y.; Zhang, L.; Wang, J.-S.; Zang, S.-Q.; Li, Z.-J. Indirect Z-scheme BiOI/g-C_3N_4 photocatalysts with enhanced photoreduction CO_2 activity under visible light irradiation. *ACS Appl. Mater. Interfaces* **2016**, *8*, 3765−3775.
(48) Khan, A.; Alam, U.; Raza, W.; Bahnemann, D.; Muneer, M. One-pot, self-assembled hydrothermal synthesis of 3D flower-like CuS/g-C_3N_4 composite with enhanced photocatalytic activity under visible-light irradiation. *J. Phys. Chem. Solids* **2018**, *115*, 59−68.
(49) Hou, Y.; Li, J.; Wen, Z.; Cui, S.; Yuan, C.; Chen, J. N-doped graphene/porous g-C_3N_4 nanosheets supported layered-MoS_2 hybrid as robust anode materials for lithium-ion batteries. *Nano Energy* **2014**, *8*, 157−164.
(50) Akhundi, A.; Badiei, A.; Ziarani, G. M.; Habibi-Yangjeh, A.; Muñoz-Batista, M. J.; Luque, R. Graphitic carbon nitride-based photocatalysts: toward efficient organic transformation for value-added chemicals production. *Mol. Catal.* **2020**, *488*, 110902.
(51) Rameshbabu, R.; Ravi, P.; Sathish, M. Cauliflower-like CuS/ZnS nanocomposites decorated g-C_3N_4 nanosheets as noble metal-free photocatalyst for superior photocatalytic water splitting. *Chem. Eng. J.* **2019**, *360*, 1277−1286.
(52) Wei, X.; Zhu, G.; Fang, J.; Chen, J. Synthesis, characterization, and photocatalysis of well-dispersible phase-pure anatase TiO_2 nanoparticles. *Int. J. Photoenergy* **2013**, *2013*, 1.
(53) Zangeneh, H.; Zinatizadeh, A. A. L.; Habibi, M.; Akia, M.; Hasnain Isa, M. Photocatalytic oxidation of organic dyes and pollutants in wastewater using different modified titanium dioxides: A comparative review. *J. Ind. Eng. Chem.* **2015**, *26*, 1−36.
(54) Akhundi, A.; Habibi-Yangjeh, A.; Abitorabi, M.; Rahim Pouran, S. Review on photocatalytic conversion of carbon dioxide to value-added compounds and renewable fuels by graphitic carbon nitride-based photocatalysts. *Catal. Rev.* **2019**, *61*, 595−628.
(55) Shekofteh-Gohari, M.; Habibi-Yangjeh, A.; Abitorabi, M.; Rouhi, A. Magnetically separable nanocomposites based on ZnO and their applications in photocatalytic processes: a review. *Crit. Rev. Environ. Sci. Technol.* **2018**, *48*, 806−857.
(56) Zhang, J.; Yu, J.; Zhang, Y.; Li, Q.; Gong, J. R. Visible light photocatalytic H_2-production activity of CuS/ZnS porous nanosheets based on photoinduced interfacial charge transfer. *Nano Lett.* **2011**, *11*, 4774−4779.
(57) Ayodhya, D.; Venkatesham, M.; Santoshi Kumari, A.; Reddy, G. B.; Ramakrishna, D.; Veerabhadram, G. Photocatalytic degradation of dye pollutants under solar, visible and UV lights using green synthesized CuS nanoparticles. *J. Exp. Nanosci.* **2016**, *11*, 418−432.
(58) Alhaddad, M.; Shawky, A. Superior photooxidative desulfurization of thiophene by reduced graphene oxide-supported MoS_2 nanoflakes under visible light. *Fuel Process. Technol.* **2020**, *205*, 106453.

https://doi.org/10.1021/acsomega.1c00697
ACS Omega 2021, 6, 8717−8725